JPhys Materials

PAPER • OPEN ACCESS

Incommensurate crystal structure, thermal expansion study and magnetic properties of (dimethylimidazolium)$_2$[Fe_2Cl_6(μ-O)]

To cite this article: Fabio Scé *et al* 2020 *J. Phys. Mater.* **3** 015002

JPhys Materials

OPEN ACCESS

RECEIVED
28 June 2019

REVISED
28 August 2019

ACCEPTED FOR PUBLICATION
6 September 2019

PUBLISHED
28 October 2019

PAPER

Incommensurate crystal structure, thermal expansion study and magnetic properties of (dimethylimidazolium)$_2$[$Fe_2Cl_6(\mu$-O)]

Fabio Scé[1], Palmerina González-Izquierdo[1,2], Israel Cano[3,4,8], Garikoitz Beobide[5], Oscar Fabelo[2], Bruno J C Vieira[6], João C Waerenborgh[6], Oriol Vallcorba[7], Oscar Castillo[5,8] and Imanol de Pedro[1,8]

[1] CITIMAC, Facultad de Ciencias, Universidad de Cantabria, 39005 Santander, Spain
[2] Institut Laue-Langevin, BP 156X, F-38042 Grenoble Cedex, France
[3] School of Chemistry, University of Nottingham, NG7 2RD, Nottingham, United Kingdom
[4] Departamento de Física Aplicada, Facultad de Ciencias, Universidad de Cantabria, 39005 Santander, Spain
[5] Departamento de Química Inorgánica, Facultad de Ciencia y Tecnología, Universidad del País Vasco, UPV/EHU, Apartado 644, E-48080, Bilbao, Spain
[6] Universidade de Lisboa, Centro de Ciéncias e Tecnologias Nucleares (C2TN), Instituto Superior Técnico, EN 10 (km 139.7), 2695-066 Bobadela, Portugal
[7] ALBA Synchrotron Light Source, Cerdanyola del Valleś, Barcelona, Spain
[8] Authors to whom any correspondence should be addressed.

E-mail: israel.canorico@unican.es, oscar.castillo@ehu.eus and depedrovm@unican.es

Keywords: halometallate complex, incommensurate crystal structure, thermal expansion studies, magnetic properties

Supplementary material for this article is available online

Abstract

A thorough characterization of the title compound, (dimim)$_2$[$Fe_2Cl_6(\mu$-O)], consisting of a (μ-oxido)-bridged binuclear iron(III) complex and 1,3-dimethylimiazolium (dimim) cation, has been performed using a wide range of techniques. The room temperature disordered crystal structure of this compound transits to an incommensurately modulated crystal structure at 100 K; to our knowledge, the first one found for an imidazolium halometallate complex. The crystal structure was solved in the superspace group P$\bar{1}(/\alpha/\beta/\gamma)0$ with modulation vector $\mathbf{q} = 0.1370(10)\ \ 0.0982(10)\ \ 0.326(2)$ at 100 K. Variable temperature synchrotron powder x-ray diffraction showed the presence of satellite peaks in addition to the main diffraction peaks up to 208 K. Furthermore, a thermal expansion study was performed with this technique from 100 to 383 K (near of its melting point) adressing questions about the nature and consequences of the ion self-assembly of this (μ-oxido)-bridged binuclear iron(III) complex, as well as the molecular motion of the imidazolium cation within the crystalline structure as a response to the temperature effect. Finally, we present a deep magnetic study based on magnetic susceptibility, magnetization and Mössbauer measurements, where the strong antiferromagnetic exchange coupling detected is due to the occurrence of a μ-oxido bridge between the Fe(III), giving rise to an intra-dimeric antiferromagnetic exchange coupling of –308 cm^{-1}.

1. Introduction

A common class of halometallate complex is the subgroup formed by a metal complex anion (with the same or different halide atom) and an imidazolium cation. The acidic character of these compounds [1, 2] can be a feature related to one of the anions, or to both of them. Moreover, depending on their cation/anion compositions, these complexes can be classified either as Lewis acidic materials, with the capability to act as electron pair acceptors (the anion is generally responsible for this type of acidity), or as Brønsted acidic compounds, in which the acidity is due to ionizable protons either to the cation or to the anion. The upper limit of the acidity achievable for any halometallate compound is the solubility of the metal halide in the corresponding organic cation salt. In the case of chlorometallate complexes, several negatively charged species are often present in equilibrium depending on the metal chloride to organic salt ratio. In chloroferrate(III)

compounds, this is constrained by the limited ability of Fe(III) to form dimeric $[Fe_2Cl_7]^-$ anions. Indeed, neutral chloroferrate(III) complexes are the most traditional and widely studied [3]. In contrast to other acidic systems, these compounds are relatively moisture-stable in liquid and solid states. In addition, they possess a latent acidity (the presence of water causes shifts in anion equilibrium) comparable to those containing chloroaluminates. Taking advantage of this acidity, moisture stability, Fe and Cl abundance, ability to dissolve a wide range of organic compounds and magnetic properties [4–8], chloroferrate(III) complexes show many applications [9]. They are especially useful as catalysts for a wide variety of transformations including glycosidation [10], Michael addition [11], desulfurization [12], CO_2 fixation into cyclic carbonates [13], Friedel Crafts acylation [14], for benzylation of various arenes/heteroarenes into the diarylmethanes [15], for Lewis rechargeable batteries [16] or glycolysis of polyethylene terephthalate (PET) waste [17, 18].

Searching for novel imidazolium- based halometallate complexes, we have recently synthetized a dinuclear 1,3-dimethylimidazolium (μ-oxido)bis[trichloridoferrate(III)] complex, $(dimim)_2[Fe_2Cl_6(\mu\text{-}O)]$, as an alternative to classic mononuclear halometallate type compounds [19]. This complex was obtained through addition of H_2O and triethylamine to a solution of (dimim)$[FeCl_4]$[6] in methanol:heptanol under continuous agitation. It is worth noting that [Fe–O–Fe] type halometallate complexes has been synthesized by a wide variety of methods, in many instances as a serendipitously obtained side product [20]. On the contrary, this is a straightforward route that would allow the large-scale synthesis of this type of compound.

To date, *ca.* 50 structures containing the dinuclear $[Fe_2Cl_6(\mu\text{-}O)]^{2-}$ unit have been published in the Cambridge Structural Database [21]. The moiety was first reported in 1978 by Drew *et al* in a study describing the synthesis, crystal structure and magnetic properties of $(Hpy)_2[Fe_2Cl_6(\mu\text{-}O)]$ (Hpy = pyridinium) [20]. Since then it has become an important example in the coordination chemistry of trivalent iron. The oxido- and hydroxido-bridged diiron complexes are relevant in several enzymes [22, 23] involved in reversible dioxygen binding, for instance, nitrogenase [24] and non-heme Fe oxygenase [25]. Moreover, the dinuclear $[Fe_2Cl_6(\mu\text{-}O)]^{2-}$ unit is also very interesting from a physical point of view because its magnetic properties and stability (diferric form) have served in the past decade as a paradigm for strong intramolecular antiferromagnetic spin exchange coupling between two high-spin ferric ions mediated by an oxido-bridge [26, 27] tending to be antiferromagnetic [28].

Regarding the structural characterization, there is a lack of published research papers based on experimental research about the effect of temperature on their crystalline structures. Concretely, these complexes based on imidazolium cation display a wide variety of interactions, ranging from nonspecific and isotropic forces, weak ones (e.g., van der Waals (vdW), solvophobic, dispersion forces) and strong ones (Coulombic), to specific and anisotropic forces (e.g., hydrogen bonding, halogen bonding, dipole−dipole, magnetic dipole, electron pair donor/acceptor interactions). The competition among the aforementioned interactions could drive to structural phase transitions as observed in neutral chloroferrate(III) complexes, mainly due to order-disorder phenomena or the libration of the imidazolium cation [3–8].

Coming back to the aforementioned $(dimim)_2[Fe_2Cl_6(\mu\text{-}O)]$ [19], we also reported structural details of its crystal structure at 293 K which is featured by a structural disorder that hinders getting deeper insights into the fundamental molecular details that dominate properties such as magnetic behavior. With all of this in mind, herein we present both (1) the elucidation of the low temperarure single-crystal x-ray incommensurate structure within its thermal expansion process and (2) an exhaustive physical characterization of the title compound by the use of a wide variety of techniques, including differential scanning calorimetry, thermogravimmetric analyses, Raman spectroscopy, DC magnetic susceptibility and magnetization, and Mössbauer spectroscopy measurements. We think that this work could be of use in understanding on a molecular level the physical/chemical properties of the (μ-oxido)bis[trichloridoferrate(III)] halometallate complexes.

2. Experimental details

2.1. Thermal analysis

Differential scanning calorimetry (DSC) analyses of $(dimim)_2[Fe_2Cl_6(\mu\text{-}O)]$ were performed on a Mettler-Toledo (DSC822) from 25 to 180 °C under nitrogen atmosphere at heating rate of 5 °C min^{-1}. For this experiment, *ca.* 7 mg of powder sample were thermally treated and blank runs were performed. Thermogravimetric analyses (TGA) were carried out on a TA instruments Discovery at a heating rate of 10 °C min^{-1} in a temperature range from 20 °C to 800 °C under synthetic air in a platinum crucible.

2.2. Single-crystal x-ray diffraction and structure determination

The crystal structure of $(dimim)_2[Fe_2Cl_6(\mu\text{-}O)]$ was determined by single-crystal x-ray diffraction (SCXRD). Data were collected using Cu-Kα radiation (1.5418 Å) in an Agilent Technologies Supernova diffractometer at 100 K. The data reduction was done with the CrysAlis PRO program [28]. Data were corrected for Lorentz and

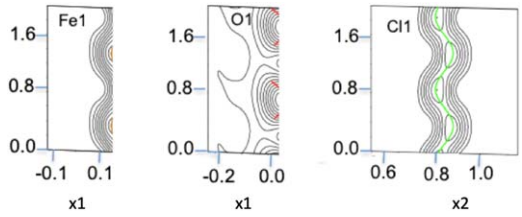

Figure 1. Positional modulation of Fe1, O1 and Cl1 atoms in $(dimim)_2[Fe_2Cl_6(\mu\text{-}O)]$ as functions of the inernal *x4* axis through the superspace.

polarization effects. The single crystal data acquisition performed showed clear signs of an incommensurate crystal structure. Careful examination of the peaks positions extracted from the CCD images showed the presence of satellite peaks in addition to the main reflections (figure S1 is available online at stacks.iop.org/JPMATER/3/015002/mmedia). The main reflections were indexed using a triclinic unit cell, but the satellite reflections required the use of four integers: $H = ha^* + kb^* + lc^* + mq$ with q = 0.1370(10) 0.0982(10) 0.326(2) to be indexed. The structure solution was fulfilled by charge-flipping algorithm [29]. (CFA) using software Jana2006 and refining on F [30]. A detailed analysis of the superspace density map obtained through the charge-flipping method reveals that the bridging oxide, O1, shows a discontinuity in the modulation function which was described using a crenel function of width 0.5 (figure 1). At RT only some diffuse scattering can be observed apart from the main reflections on the diffraction frames. Therefore, the structure was solved by direct methods using the SIR92 program [31] and refined by full matrix least-squares on F^2 including all reflections (SHELXL97) [32]. The crystal solution required the presence of a disordered μ-oxido bridge over two positions related by a symmetry center. All non-hydrogen atoms were refined anisotropically but the anisotropic thermal displacement parameters of most atoms were unusually high and elongated. H atoms were included at calculated positions and treated as riding atoms with isotropic thermal motion related to its parent atom. All calculations for the latter were performed using the WINGX crystallographic software package [33]. Crystallographic data and details of the structure determination and refinement for the complex are summarized in table 1. Crystallographic information (CIF) files are available in the supporting information (SI).

2.3. Variable temperature synchrotron x-ray powder data collection

Synchrotron x-ray powder diffraction (SR-XRPD) measurements were performed at the high resolution station of the MSPD beamline (BL04) at ALBA synchrotron [34]. The sample was introduced into a 0.7 mm glass capillary and measured in transmission at E = 20 keV using the microstrip Mythen-II detector (six modules, 1280 channels/module, 50 μm/channel, sample-to-detector distance 550 mm). Temperature was controlled using an Oxford Cryosystems Series 700 Cryostream. Data from 2 to 45° (2θ) were collected during a 5 K min^{-1} ramp from 100 to 400 K every 30 s. Exact wavelength for the experiments was 0.619 69 Å determined from a Si NIST-640d reference.

2.4. Raman spectroscopy

The non-polarized Raman spectra of $(dimim)_2[Fe_2Cl_6(\mu\text{-}O)]$ was recorded in backscattering geometry with a Horiba T64000 triple spectrometer with the same protocol of reference [35].

2.5. Magnetic measurements.

Temperature dependence of the magnetic susceptibility measurements for $(dimim)_2[Fe_2Cl_6(\mu\text{-}O)]$ were performed using a standard QD MPMS magnetometer by heating from 2 to 300 K at 10 KOe after cooling in either the presence (field cooling, FC) or the absence (zero field cooling, ZFC) of the applied field. Magnetization as a function of field (H) was measured using the same magnetometer in the $-50 \leqslant H/kOe \leqslant 50$ at 2 K. ^{57}Fe Mössbauer measurements were recorded between 295 and 4 K with the same protocol of reference [36]. The spectra were fitted to Lorentzian lines using a non-linear least-squares method [37].

3. Results and discussions

3.1. Thermal analysis

TGA curves show that $(dimim)_2[Fe_2Cl_6(\mu\text{-}O)]$ starts to decompose at 196 °C (figure 2(a)). DSC curves display a melting point of *ca.* 98 °C upon heating (figure 2(b)), which was corroborated by means of variable temperature SR-XRPD experiments (see below). Therefore, the complex reported herein could be considered as a

Table 1. Crystallographic data and structure refinement details of $(dimim)_2[Fe_2Cl_6(\mu\text{-}O)]$ at 100 K.

Chemical formula	$(C_5H_9N_2)[Fe_2Cl_6(\mu\text{-}O)]$
Mr	534.7
Formula units	1
Radiation type	Cu Kα
Wavelength (Å)	1.541 84
Temperature (K)	100(2)
Crystal system, space group	Triclinic, P$\bar{1}$ ($\alpha\beta\gamma$)0
a (Å)	7.1967(6)
b (Å)	7.4456(6)
c (Å)	10.4488(7)
α (°)	103.341(6)
β (°)	100.037(7)
γ (°)	92.582(7)
V (Å^3)	534.31(7)
Density (g/cm^3)	1.662
Abs coeff μ (mm^{-1})	17.845
Modulation vector	0.1370(10) 0.0982(10) 0.326(2)
Max. order of satellites	1
Range of h, k, l, (m)	$-8 \leqslant h \leqslant 9$ $-9 \leqslant k \leqslant 8$ $-13 \leqslant l \leqslant 11$ $-1 \leqslant m \leqslant 1$
No. of measured and unique reflns	13 060, 6565
No of parameters	314
No. of obsd reflns	4901
No. of obsd main reflns	1863
No. of obsd first-order satellites	3038
Criterion for obs reflns	$I > 3\sigma(I)$
R_{int}	0.0592
Goodness of fit (S)	2.53
R, wR (obs reflns)	0.1039, 0.1238
R, wR (main reflns)	0.1037, 0.1240
R, wR (satellite reflns)	0.1040, 0.1233
$\Delta\rho_{max/min}$ (e · Å^{-3})	0.89/−0.65

paramagnetic ionic liquid (MIL) which, according to the literature, is defined as a paramagnetic salt with a melting point below 100 °C [38]. In fact, similar melting temperature values have been observed in previously reported halometallates, such as $(pyprmim)_2[Fe_2Cl_6(\mu\text{-}O)]$ (pyprmim: 1-(1-pyridinium-yl-propyl)-3-methylimidazolium, T_m: 104 °C) [26] and other (μ-oxo)bis[trichloroferrate(III)] dianion salts [39]. The cooling curve of the thermogram reveals a marked delay in the crystallization peak (supercooling: 46 °C) which is similar in magnitude to that observed in hydrated inorganic salts [40]. It is worth noting that the shape of the cooling peak could suggest the occurrence of a solid-solid transition immediately after crystallization. However, after this cooling peak, the low temperature phase shows the crystal structure as that found in the fresh sample (see following section). Finally at a temperature near of −90 °C the DSC curve (see inset of figure 2(b)) display a transition, probably due to the change from a incommensurate crystal structure to a disordered one (see below).

3.2. Structural characterization

As we commented above, we recently reported the synthesis of $(dimim)_2[Fe_2Cl_6(\mu\text{-}O)]$. Such a complex was employed as catalyst for the degradation of PET under conventional and microwave-assisted heating. Furthermore we also described the RT crystal structure of $(dimim)_2[Fe_2Cl_6(\mu\text{-}O)]$ (space group: *P*–1; cell parameters: $a = 7.3221$ Å, $b = 7.5071$ Å, $c = 10.4916$ Å and $\alpha = 102.996°$ $\beta = 100.472°$ $\gamma = 92.433°$). At this temperature, its crystal structure is built up by dinuclear (μ-oxido)bis(trichloridoferrate)(2–) anionic complexes and 1,3-dimethylimiazolium cations. The asymmetric unit consists of one organic cation and half metal complex. The symmetry center, located in the middle of the intermetallic Fe···Fe axis, entails the disorder of the bridging oxygen atom into two symmetry-related positions with an occupation factor of 0.5 each.

However, the data collection at cryogenic temperatures (table 1) has allowed us to realize that this chloroferrate(III) compound presents an interesting structural feature as it transits from a disordered crystal

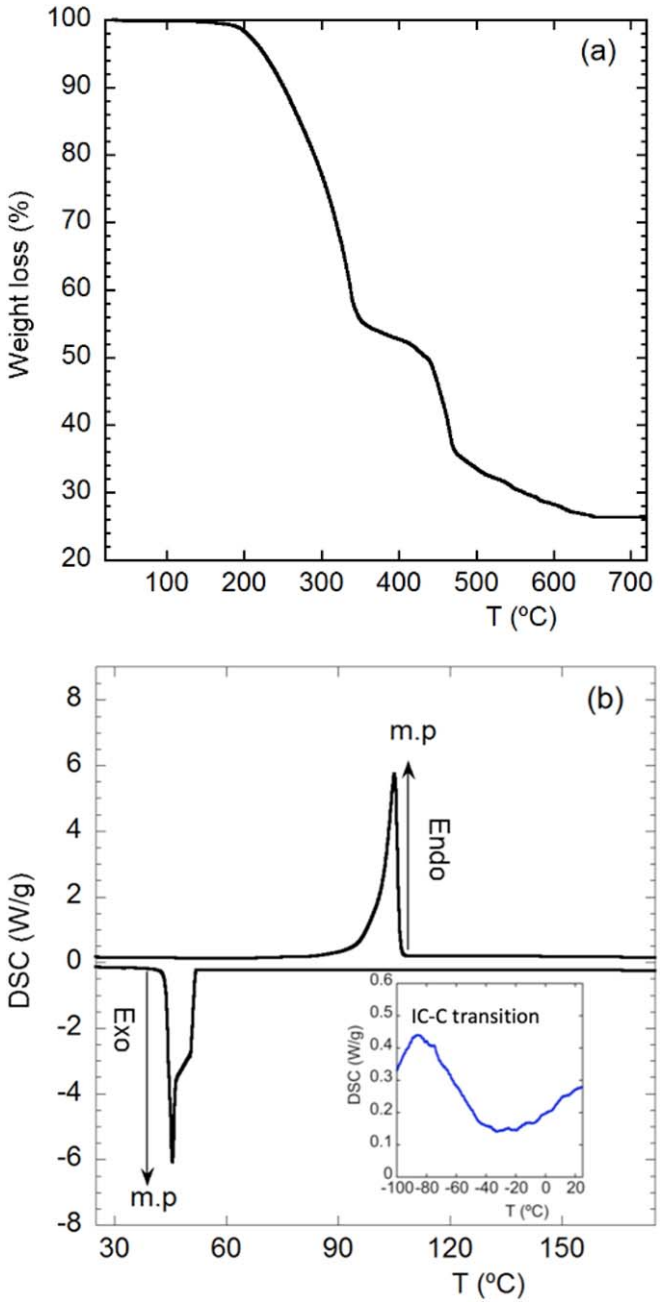

Figure 2. (a) TGA curve recorded in air atmosphere. (b) DSC thermogram of $(dimim)_2[Fe_2Cl_6(\mu\text{-}O)]$. 2nd heating and cooling cycle. Heating rate 5 K min^{-1}. The inset shows the enlargement of the low temperature crystal phase transition.

structure at room temperature to an incommensurate ordering at 100 K. Selected bond lengths and angles for the coordination environment of Fe(III) at both temperatures are presented in table 2, while those corresponding to the imidazolium cations are gathered in the SI (table S1). Bond parameters corresponding to the metal center are similar to those found in previously described $[Fe_2X_6(\mu\text{-}O)]^{2-}$ (X: halide anion) type complexes [26, 39, 41].

In order to ease the understanding of the structural modulation and its origin, firtsly the average crystal structure is described in the next two paragraphs. The coordination polyhedron of Fe(III), defined by the Cl_3O donor set, resembles a slightly distorted tetrahedron according to continuous shape measurements ($S_{Td} = 0.82$) [42]. With regard to the geometry of the dinuclear entity, the oxide bridge sets a bended geometry with Fe1–O1–Fe1(i) angle of 158º and Fe1···Fe1(i) distance of 3.475 Å, which are in agreement with previously reported distances [24–26]. Furthermore, in order to reduce steric hindrance, the bridged trihalidoferrate groups display a staggered conformation.

Thus, at RT, the crystal structure (figure 3(a)) is sustained by electrostatic attraction forces established between the ionic entities and through an intricate network of non-covalent interactions, occurring between

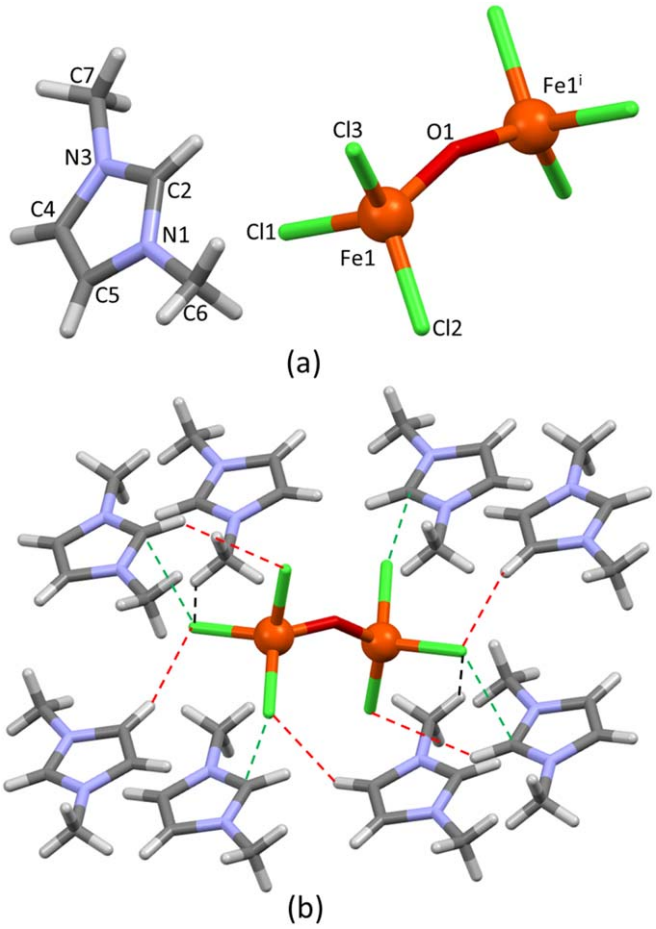

Figure 3. (a) Constituents of the crystal structure showing the atom labelling.(b) Relevant non-covalent interactions around the dinuclear complex. Hydrogen bonding due to imidazolium aromatic C–H and methyl groups are represented in red and green dashed lines, respectively. The halide$\cdots\pi$ interactions are depicted in black dashed lines.

Table 2. Selected bond lengths and angles of $[Fe_2Cl_6(\mu\text{-}O)]^{2-}$ anion.

T(K)		100(2)		
Bond lengths (Å)	293(2) [19]	Average	Minimum	Maximum
Fe1–O1	1.848(2)	1.77(4)	1.75(6)	1.81(6)
Fe1–Cl1	2.217(2)	2.226(3)	2.218(3)	2.238(3)
Fe1–Cl2	2.211(2)	2.225(3)	2.196(3)	2.253(3)
Fe1–Cl3	2.206(4)	2.204(4)	2.159(4)	2.250(4)
Angles (°)				
O1–Fe1–Cl1	103.1(6)	112.0(8)	109.9(8)	113.0(8)
O1–Fe1–Cl2	104.3(7)	112.5(8)	109.7(8)	118.7(7)
O1–Fe1–Cl3	124.5(5)	108.1(8)	102.7(7)	111.1(8)
Cl1–Fe1–Cl2	106.1(1)	106.1(1)	104.5(1)	107.1(1)
Cl1–Fe1–Cl3	110.3(1)	110.7(1)	109.6(1)	111.6(1)
Cl2–Fe1–Cl3	107.2(2)	108.0(1)	107.3(1)	109.0(1)
Fe1-O1-Fe1(i)	154.5(8)	158(3)	155(2)	165(4)

iron(III) complexes and organic moieties (figure 3(b) and table S1). These interactions comprise C_{ar}–H hydrogen bonding (C4–H4$\cdots$Cl2, C5–H5$\cdots$Cl1), halide$\cdots\pi$ interactions (Cl1$\cdots$C2) and halide$\cdots$methyl interactions (Cl2$\cdots$H6–C6; Cl1$\cdots$H7–C7), which have also been observed in other imidazolium ILs. Indeed, such interactions have also been observed for the (dimim)[$FeCl_4$] precursor [6] and other imidazolium ILs [43]. In addition to the aforementioned non-covalent interactions, the crystal packing of analogous (im)[FeX_4] type ILs (im: imidazolium derivative; X: halide ligand) implies non-covalent interactions between metal complexes.

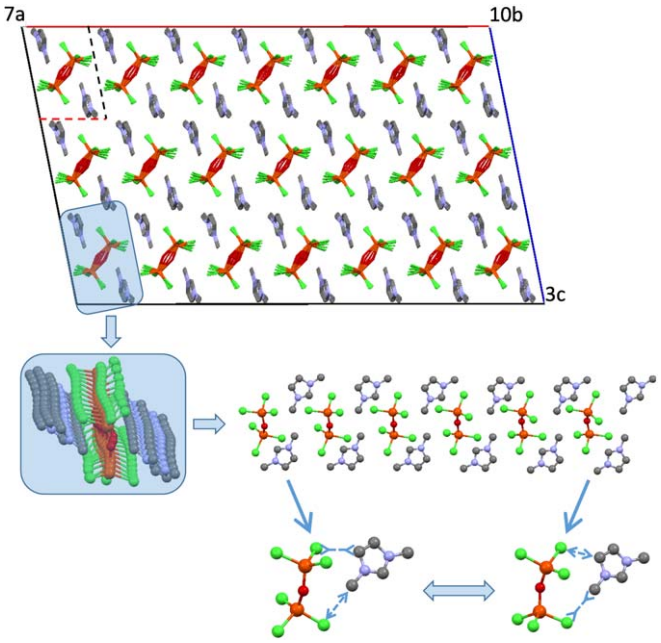

Figure 4. Approximant supercell ($7a \times 10b \times 3c$) of $(dimim)_2[Fe_2Cl_6(\mu\text{-}O)]$ at 100 K, showing the supramolecular modulation of the atomic positions and the competing supramolecular interactions probably responsible of the modulation.

These specific interactions play a crucial role in the laminar packing of the ionic entities and also in their magnetic structure, as in these cases it is governed by Fe–Cl···Cl–Fe type superexchange pathways [3, 6, 8]. On the contrary, the ionic charge of $[FeCl_6(\mu\text{-}O)]^{2-}$ involves two imidazolium cations per formula instead of one. As a consequence, each metal complex is surrounded by eight cations (figure 3(b)), which precludes direct interactions between them. It is also worth to mention that there is no evidence of direct supramolecular interactions between imidazolium cations.

As previously stated, the single crystal data acquisition performed at 100 K showed clear signs of an incommensurate crystal structure that required the inclusion of a modulation vector to index the satellite reflections. The atom positions affected by the structural modulation could be viewed by using the commensurate approximant and drawing an approximant supercell. We could see that the vector $0.136a^* + 0.098b^* + 0.326c^* \approx 1/7a^* + 1/10b^* + 1/3c^*$ and thus a $7a \times 10b \times 3c$ could be drawn to get an approximate description of the modulated structure, as shown in figure 4.

Interestingly, in the modulated structure, the bridging oxide is no longer disordered but oscilates between those two positions observed in the RT model following the modulation wave. The modulation seems to be induced by the presence of two competing supramolecular interactions between the dimeric $[Cl_3FeOFeCl_3]^{2-}$ complex entity and the 1,3-dimethylimidazolium cations: C7–H7···Cl1 and C4–H4···Cl2 as can be seen at the bottom of figure 4 (bottom). The intramolecular geometry and distances of the dimethylimidazolium cation does not allow to maximize both interactions simultaneously, thus generating a structural instability that leads to an incommensurate crystal structure at low temperatures due to the thermal expansion effects. However, the shrinkage of the unit cell volume between RT and 100 K is ca. 1% with a slightly anisotropic expansion along the *a*-axis. Apart from that, the main structural feature is the significantly shorter Fe–O bond distances at 100 K (1.77 Å versus 1.85 Å). These subtle variation in the supramolecular interactions explains the difficulty to obtain incommensurate structures on these imidazolium-based system, where the large mobility of the counterion preclude in most of the cases arriving to this situation of quasi-equilibrium.

Once the crystal structure was elucidated, SR-XRPD experiments were performed in order to follow the thermal evolution (see figure S2) of differents crystal parametres. On one hand, the temperature evolution of the SR-XRPD patterns between 100 and 400 K (see figure 5) shows the appearance of additional elastic intensity at temperatures below around 210 K, denoting the onset of the incommensurate structure.

These additional elastic intensities can be indexed with the propagation vector $\mathbf{q} = 0.137\,07(16)\ \ 0.100\,69(9)\ \ 0.322\,32(22)$ at 100 K in good agreement with SCXRD data (see figure 6). Sequential refinements against these data were performed using the FullProf suite [44] to follow the evolution of this parameter in the range from 100 to 208 K. The temperature dependence is given in figure S3 showing an almost linear behaviour of the propagation vector up to 200 K. Later, it is modificated up to a value of $\mathbf{q} = 0.128\,14(68)\ \ 0.098\,42\,(13)\ \ 0.335\,38(16)$ at 208 K.

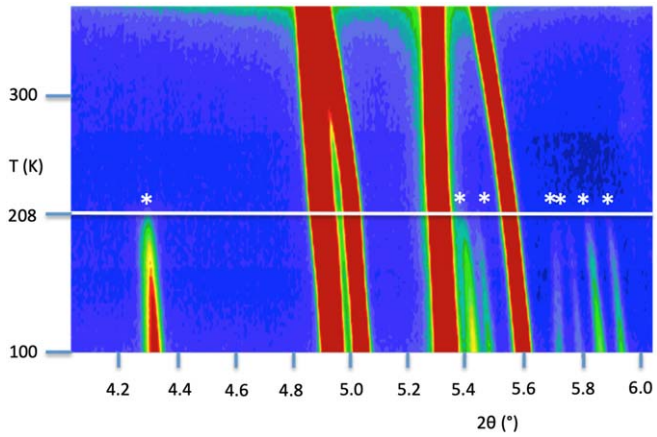

Figure 5. 2D contours of the temperature dependence of the selected 2θ region of SR-XRPD patterns between 100 and 380 K. The (*) dots show several satelite peaks. The line at 208 K shows the temperature associated with the change of the crystal structure.

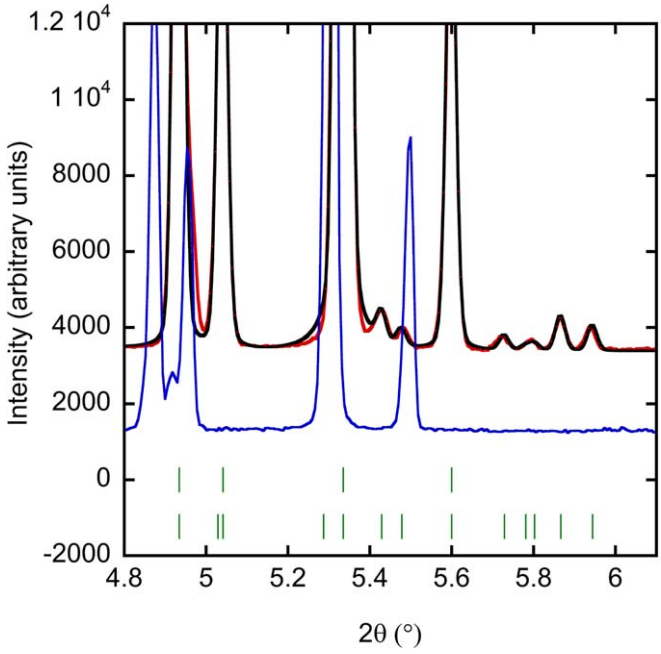

Figure 6. Observed SR-XRPD profiles of $(dimim)_2[Fe_2Cl_6(\mu\text{-}O)]$ at 100 K (red) and RT (blue). Calculated (black solid line) powder diffraction patterns at 100 K obtained with the MSPD beamline (BL04) at ALBA synchrotron. Positions of the Bragg reflections for the nuclear structure (first row) and modulation vector (second row) are presented.

On the other hand, the fitting of the experimental patterns reveals that the cell parameters evolve anisotropically up to the melting point of the sample, with the *a* lattice increasing nearly 0.23 Å and the *b* and *c* axes growing by 0.12 and 0.06 Å, respectively (figure 7(a)). Moreover, the β parameter is the only angle that increases with temperature (0.81°), whereas α and γ angles are reduced by 0.62° and 0.28°, respectively (figure 7(b)). The cell volume increases in ≈30 $Å^3$. All length parameters display a positive thermal expansion, showing a change of tendency in the slope around 210 K due to the transits from an incommensurate crystal structure to disordered one. Finally, cooling powder x-ray diffraction data confirms the aforementioned supercooling of the melted compound, as the emersion of the diffraction peaks is delayed until 40 °C. In any case, despite some widening of the diffraction peaks, the solid/liquid transition of $(dimim)_2[Fe_2Cl_6(\mu\text{-}O)]$ is reversible (figure S4).

3.3. Raman spectroscopy.

The structural characterization of the complex was also performed by Raman spectroscopy, as this technique offers one of the most rewarding and simple means for studying the bonding and type of anionic species in halometallate

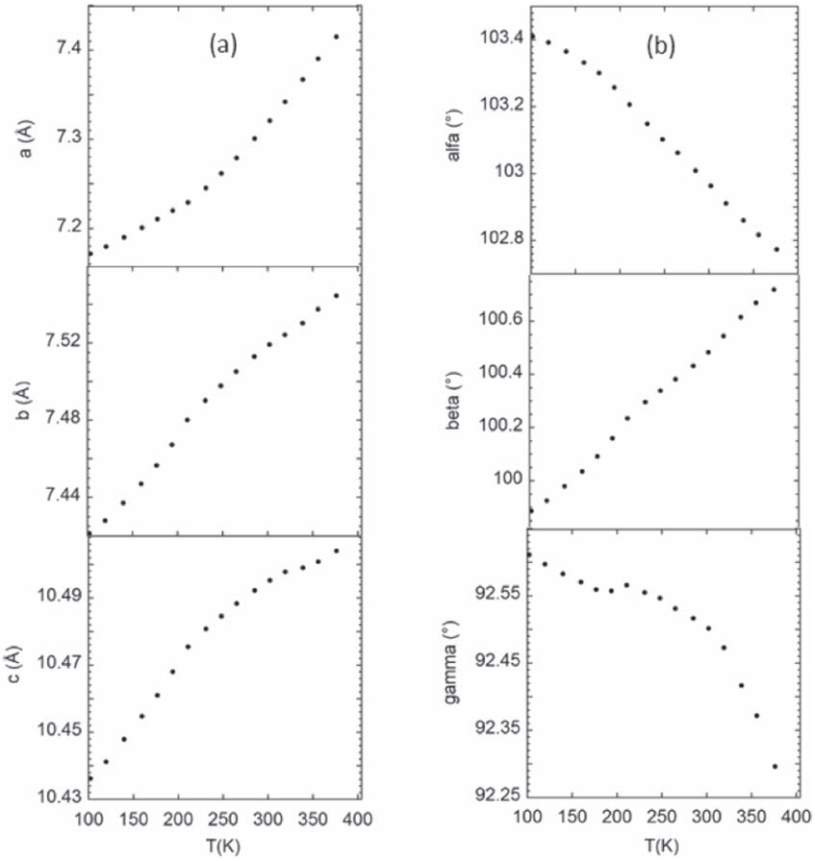

Figure 7. (a) Evolution of *a*, *b* and *c*, (b) α, β and Υ cell parameters during sample heating from 100 to 373 K.

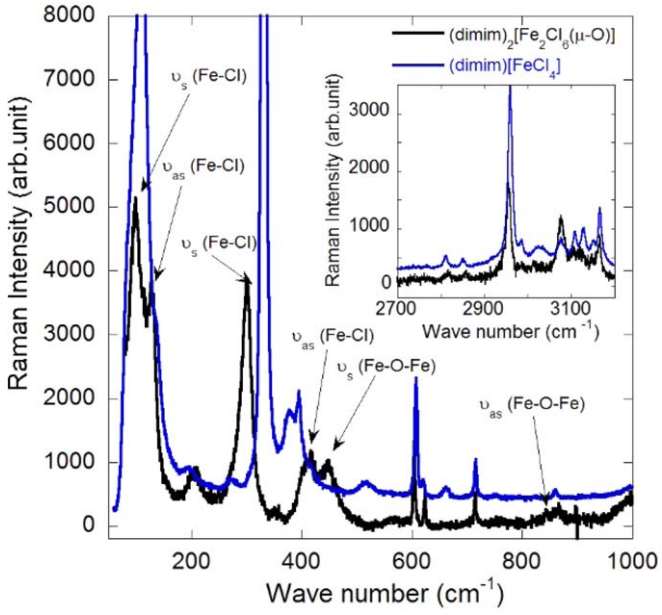

Figure 8. Raman spectra of (dimim)[$FeCl_4$] (blue) and (dimim)$_2$[Fe_2Cl_6(μ-O)] (black) in the range 50–1000 cm^{-1} and (inset) between 2700 and 3200 cm^{-1}.

compounds in a lab [4–9]. Figure 8 shows the non-polarized Raman spectra of (dimim)$_2$[Fe_2Cl_6(μ-O)] and (dimim)[$FeCl_4$] (for the comparison), between 50 and 3200 cm^{-1} at 300 K with 647 nm excitation. Neutral chloroferrate(III) [MX_4], as the precursor, display a vibrational spectra characterized by four Raman-active vibration modes in the low-frequency region. In the case of (dimim)$_2$[Fe_2Cl_6(μ-O)] these bands are shifted to higher (3 bands)

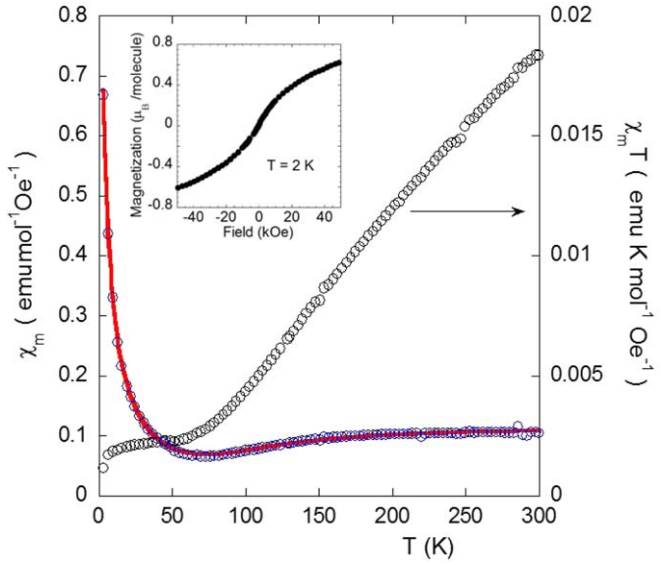

Figure 9. Temperature dependence of χ_m and χ_mT measured under 10 kOe. The solid red line represents the best fit of equation (1) (see main text). The inset shows the field dependence of the magnetization M(H), collected at 2 K.

and lower (1 band) energies and are attributed to the bending modes [$\nu_s = 98$ and $\nu_{as} = 128$ cm^{-1}] and the stretching modes [$\nu_s = 302$ and $\nu_{as} = 408$ cm^{-1}] of Fe–Cl bonds (see figure 8 and table S2, SI). In addition, the vibrational spectrum of this compound features the symmetric (medium intensity) and antisymmetric (low intensity) Fe–O–Fe stretching bands in the vicinity of 446 and 847 cm^{-1}. Indeed, the latter peaks are a fingerprint of (μ-oxido) bis(trichloridoferrate) type complexes [45]. Regarding the counterion, $(dimim)^+$, the most representative modes appear at 2700–3200 cm^{-1} (νC_{ar}–H and νC_{methyl}–H stretching; inset of figure 8) and 1000–1600 cm^{-1} (νN–C_{methyl} stretching and in-plane ring deformation). No meaningful differences are observed for Raman peak positions of the $(dimim)^+$ cation [6] when comparing the spectra of both compounds (see the inset of figure 8). Further information is gathered in table S2 (SI).

3.4. Magnetic properties

The magnetic properties of the title complex were determined over the temperature range 2–300 K on a SQUID magnetometer with an external field of 10 kOe. The plots for the magnetic susceptibility (χ_m) and the χ_mT versus T, calculated for two Fe(III) ions, are shown in figure 9. The molar magnetic susceptibility decreases from RT, accordingly to an antiferromagnetic coupling, and it reaches a minimum at *ca.* 60 K, which increases later up to 2 K. The χ_mT curve also decreases from 0.73 emu · K · mol^{-1} · Oe^{-1} at 300 K to 0.47 emu · K · mol^{-1} · Oe^{-1} at 2 K. The χ_mT value at RT is considerably lower than expected for a dinuclear species containing non-interacting Fe^{III} ($S = 5/2$) ions (8.754 emu · K · mol^{-1} · Oe^{-1}). Moreover, the effective magnetic moment, $\mu_{eff} = (8\chi_mT)^{1/2}$, was 2.41 μ_B/Fe_2, which is notably lower than the expected spin-only value of 8.37 μ_B/Fe_2 expected for two independent Fe^{III} spins ($g = 2$, $S = 5/2$). These results suggest the presence of a relatively strong intramolecular antiferromagnetic exchange interaction at RT [39].

The evolution of the molar magnetic susceptibility with temperature was analyzed using the Van Vleck equation for a $S = 5/2$ dinuclear spin model (equation (1)), derived from the spin exchange Hamiltonian $\boldsymbol{H} = -J\boldsymbol{S}_1 \cdot \boldsymbol{S}_2$ ($S_1 = S_2 = 5/2$) [39].

$$\chi = \frac{2Ng^2\beta^2}{kT}\frac{e^x + 5e^{3x} + 14e^{6x} + 30e^{10x} + 55e^{15x}}{1 + 3e^x + 5e^{3x} + 7e^{6x} + 9e^{10x} + 11e^{15x}}(1 - p) + \frac{Ng^2\beta^2S(s+1)}{3k(T - \theta)}(p) + TIP \qquad (1)$$

In equation (1), p represents the fraction of the paramagnetic impurity and $x = J/kT$, with J being the magnetic coupling constant. A term corresponding to the temperature independent paramagnetism (TIP) has been included in the model. The best fit to equation (1) gives rise to values of $J = -308(11)$ cm^{-1} and $p = 1.5$ (1) %, with TIP held constant at 500 $\times$ 10^{-6} cm^3 mol^{-1}. It is worth noting that the g value for both the mononuclear contribution and the dinuclear units was fixed to 2.00 to avoid over-parameterization. The determined J value is in the range reported for other complexes containing the $[Fe_2OCl_6]^{2-}$ unit [26, 39]. Although there is not a clear relationship between the magnitude of antiferromagnetic exchange coupling and the Fe–O–Fe angle in $[Cl_3Fe–O–FeCl_3]^{2-}$ type complexes [27], the strength of the coupling is markedly influenced by the Fe–O bond, in such a way that the shorter the Fe–O bond distance, the stronger the magnetic

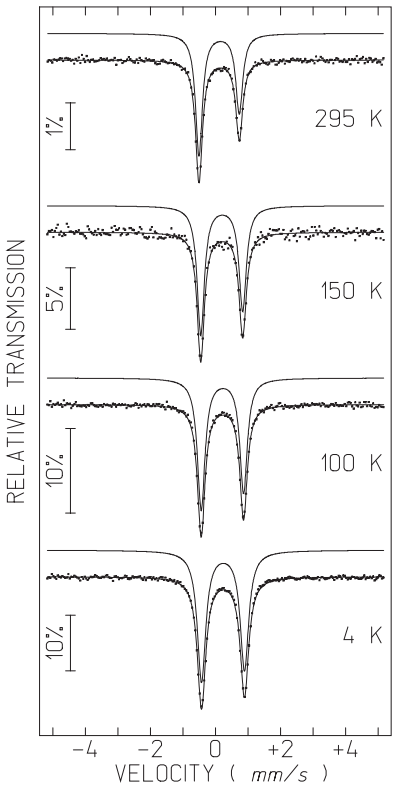

Figure 10. Mössbauer spectra of $(dimim)_2[Fe_2Cl_6(\mu\text{-}O)]$ acquired at different temperatures. The lines over the experimental points are quadrupole doublets (estimated parameters in table 2).

Table 3. Estimated parameters from the Mössbauer spectra of $(dimim)_2[Fe_2Cl_6(\mu\text{-}O)]$ acquired at different temperatures.

T (K)	IS (mm s^{-1})	QS (mm s^{-1})	Γ (mm s^{-1})	I
295	0.23	1.24	0.25	100
150	0.31	1.29	0.26	100
100	0.33	1.30	0.28	100
4.0	0.34	1.32	0.32	100

IS (mm/s) isomer shift relative to metallic α-Fe at 295 K; QS (mm/s) quadrupole splitting; Γ (mm/s) peak width; I relative area. Estimated errors $\leqslant$ 0.02 mm s^{-1} for IS, QS and Γ.

coupling. A theoretical calculation shows that the exchange coupling should be *ca.* 340 cm^{-1} for an Fe–O–Fe angle of 160° and a Fe–O bond distance of *ca.* 1.75 Å [45], which is slightly stronger than the value reported herein (308 cm^{-1}) according to its larger Fe–O bond distance [1.848(2) Å]. This behavior could be indicative of a weak ferromagnetism inside binuclear iron(III) complexes due to the antisymmetric Dzyaloshinskii–Moriya superexchange interaction.

The field dependence of magnetization M(H) collected at 2 K is displayed in the inset of figure 9. At this temperature, it tends to saturate at 50 kOe with a value of magnetization of 0.6 μ_B/formula, which is far from the expected fully saturated value of 10 μ_B for two non-interacting Fe^{III} ions. Furthermore, the magnetization shows neither a ferromagnetic component (no irreversibility in the *dM/dH*) nor signal of a metamagnetic transition in the entire applied field. Therefore, the shape of the field dependent magnetization curve is in agreement with a small rotation of the dinuclear units along the direction of the external applied field, but the intra-dinuclear interactions remain strongly antiferromagnetically coupled.

The Mössbauer spectra of the presented compound consists of two absorption peaks similar to those previously described for complexes containing the $[Fe_2Cl_6(\mu\text{-}O)]^{2-}$ unit and other organic cations [46, 47]. The spectrum acquired at 295 K (figure 10) is asymmetric, with the intensity of the high velocity peak being lower than the low velocity peak. The widths of both peaks are equal within the experimental error. This contrasts with the spectrum of $(BzlMe_3N)_2[Fe_2Cl_6(\mu\text{-}O)]$ ($BzlMe_3N$: benzyltrimethylammonium) reported by Molins *et al* [47]

which contains a small amount of impurities. Furthermore, the peaks in the spectrum of the complex at RT are narrow, with the same width as those of the αFe used for calibration. It is therefore unlikely that the asymmetry results from the presence of more than one doublet with different parameters and seems rather due to either texture effects or to the Goldanskii–Karyagin effect. Considering that the asymmetry of the doublets strongly decreases with decreasing temperature, such an asymmetry is very likely caused by the Goldanskii–Karyagin effect, as suggested by Petridis *et al* for $(BzPh_3P)_2[Fe_2Cl_6(\mu\text{-}O)]$ ($BzPh_3P$: benzyltriphenylphosphonium) [48].

The isomer shift (IS) relative to metallic αFe at 295 K and the quadrupole splitting (QS) estimated for the single doublet fitted to the spectra are similar to those described for analogous compounds (table 3) [48, 49]. The IS values are consistent with tetrahedrally coordinated Fe^{3+} in the $S = 5/2$ state [50] and their increase with decreasing temperature is explained by the second order Doppler shift. As expected, the IS values are slightly lower than those reported for oxido-bridged dinuclear complexes [47], in which Fe^{3+} is in an almost ideal octahedral environment. Finally, no long-range magnetic order is detected down to 4 K, in good agreement with DC magnetic susceptibility data, since the relaxation of the Fe^{3+} magnetic moments directions remains fast compared to the Mössbauer time window.

4. Conclusions

The crystal structure of (μ-oxido)bis[trichloridoferrate(III)] is sustained by an intricate network of non-covalent interactions occurring between staggered $[Fe_2Cl_6(\mu\text{-}O)]^{2-}$ anions and $(dimim)^+$ cations, and exhibits an anisotropic thermal expansion from 100 K up to its melting point. The competition among different supramolecular interactions at low temperature gives rise to an incommensurate crystal structure that translates into a structural disorder one near of 210 K. Thus, the occurrence of new reflections in the diffraction pattern at 100 K are compatible with an incommensurate structure for which an approximant supercell 210 times larger than the of RT ($V^{LT} = 7a^{RT} \times 10b^{RT} \times 3c^{RT}$) can be generated. The low temperature phase was solved using the super-space formalism, showing that the structure remain in a triclinic space group after the phase transition. Although, due to the well know ability of the (dimim) group to present displace and rotational transformation as function of the temperature, a large number of phase transition have been observed on imidazolium-based systems. However, to the best of our knowledge the $(dimim)_2[Fe_2Cl_6(\mu\text{-}O)]$ compound is the first one presenting an incommensurate structure at low temperature. Based on the RT and the LT crystal structures, the order-disorder of the μ-oxido bridge could be the trigger of this uncommon phase transition.

Furthermore, the μ-oxido bridge is not only playing on the structural phase transition but also play a fundamental role in the magnetic behavior of this compound. The Fe–O–Fe bridge provides a relatively strong antiferromagnetic exchange between the two equivalent high-spin state ($S = 5/2$) iron(III) centers, which is even observed at RT. Based on the susceptibility and Mössbauer measurements we can conclude that the magnetic behaviour is governed by the intra-dimers antiferromagnetic coupling. Due to the occurrence of this strong intra-dimers magnetic interaction, no long range magnetic ordering is detected down to 2 K.

Acknowledgments

Financial support from Universidad de Cantabria (Proyecto Puente convocatoria 2018 funded by SODERCAN_FEDER), Universidad del País Vasco/Euskal Herriko Unibertsitatea (GIU17/50 and PPG17/37) and Ministerio de Economia y Competividad (MAT2017-89239-C2-(1,2)-P). The authors gratefully acknowledge Technical and human support provided by SGIKer (UPV/EHU, MINECO, GV/EJ, ERDF, and ESF). Dr. Israel Cano thanks financial support from the European Community through a Marie Skłodowska-Curie Individual Fellowship (IF-EF; Programme/Call: H2020-MSCA-IF-2015; Proposal No: 704710–Sdchirnanocat). C2TN authors acknowledge the FCT (Portugal) support through the UID/Multi/04FeCl49/2013 project. The paper is (partly) based on results of experiments carried out at the ALBA Synchrotron Light Source in Barcelona.

Associated content

Supporting information (SI) available with Accession Codes. Crystallographic data for the structure reported in this paper have been deposited in the Cambridge Crystallographic Data Center under reference number CCDC (1918472). The data can be obtained free of charge via www.ccdc.cam.ac.uk/data_request/cif.

Author contributions

The manuscript was written through contribution of all authors. All authors have given approval to the final version of the manuscript.

Notes

The authors declare no competing financial interest.

ORCID iDs

Israel Cano https://orcid.org/0000-0003-3727-9327
Oscar Castillo https://orcid.org/0000-0002-5614-9301
Imanol de Pedro https://orcid.org/0000-0002-5581-2220

References

[1] Amarasekara A S 2016 *Chem. Rev.* **116** 6133–83
[2] Chiappe C and Rajamani S 2011 *Eur. J. Org. Chem.* **2011** 5517–39
[3] Garcia-Saiz A *et al* 2014 *Inorg. Chem.* **53** 8384–96
[4] Yoshida Y, Otsuka A, Saito G, Natsume S, Nishibori E, Takata M, Sakata M, Takahashi M and Yoko T 2005 *Bull. Chem. Soc. Jpn.* **78** 1921–8
[5] de Pedro I, Rojas D P, Albo J, Luis P, Irabien A, Blanco J A and Rodriguez Fernandez J 2010 *J. Phys. Condens. Matter* **22** 296006
[6] García-Saiz A *et al* 2014 *Chem.: Eur. J.* **20** 72–6
[7] de Pedro I, Fabelo O, García-Saiz A, Vallcorba O, Junquera J, Blanco J A, Waerenborgh J C, Andreica D, Wildes A and Fernández-Díaz M T 2016 *Phys. Chem. Chem. Phys.* **18** 21881–92
[8] González-Izquierdo P, Fabelo O, Beobide G, Vallcorba O, Sce F, Rodríguez J F, Fernández-Díaz M T and de Pedro I 2018 *Inorg. Chem.* **57** 1787–95
[9] Estager J, Holbrey J D and Swadźba-Kwaśny M 2014 *Chem. Soc. Rev.* **43** 847–86
[10] Tilve R D, Alexander M V, Khandekar A C, Samant S D and Kanetkar V R 2004 *J. Mol. Catal. Chem.* **223** 237–40
[11] Vasiloiu M, Gaertner P and Bica K 2012 *Sci. China Chem.* **55** 1614–9
[12] Ko N H, Lee J S, Huh E S, Lee H, Jung K D, Kim H S and Cheong M 2008 *Energy Fuels* **22** 1687–90
[13] Leu M K, Vicente I, Fernandes J A, de Pedro I, Dupont J, Sans V, Licence P, Gual A and Cano I 2019 *App. Catal. B Environ.* **245** 240–50
[14] Valkenberg M and Hölderich W 2001 *Appl. Catal.*, A **215** 185–90
[15] Gao J, Wang J-Q, Song Q-W and He L-N 2011 *Green Chem.* **13** 1182–6
[16] Katayama Y, Konishiike I, Miura T and Kishi T 2002 *J. Power Sources* **109** 327–32
[17] Cot S, Leu M K, Kalamiotis A, Dimitrakis G, Sans Sangorrin V, de Pedro I and Cano I 2019 *ChemPlusChem.* **84** 1–9
[18] Wang Q, Geng Y, Lu X and Zhang S 2015 *ACS Sustain. Chem. Eng.* **3** 340–8
[19] Scé F, Cano I, Martin C, Beobide G, Castillo Ó and de Pedro I 2019 *New J. Chem.* **43** 3476–85
[20] Drew M, McKee V and Nelson S M 1978 *J. Chem. Soc., Dalton Trans.* **0** 80–4
[21] Groom C R, Bruno I J, Lightfoot M P and Ward S C 2016 *Acta Crystallogr.* B **72** 171–9
[22] Kurtz D M Jr 1990 *Chem. Rev.* **90** 585–606
[23] Gorun S M and Lippard S J 1991 *Inorg. Chem.* **30** 1625–30
[24] Girma K B, Lorenz V, Blaurock S and Edelmann F T 2008 *Inorganica Chim. Acta* **361** 346–8
[25] Li F, Wang M, Ma C, Gao A, Chen H and Sun L 2006 *Dalton Trans.* **28** 2427–34
[26] Haselhorst G, Wieghardt K, Keller S and Schrader B 1993 *Inorg. Chem.* **32** 520–5
[27] Chen Z, Xu Z, Zhang L, Yan F and Lin Z 2001 *J. Phys. Chem. A* **105** 9710–6
[28] Oxford Diffraction 2008 *CrysAlis RED*. (Abingdon, England: Oxford Diffraction Ltd)
[29] Palatinus L and Chapuis G 2007 *J. Appl. Crystallogr.* **40** 786–90
[30] Petříček V, Dušek M and Palatinus L 2014 *Z. Kristallogr. Cryst. Mater.* **229** 345–52
[31] Altomare A, Cascarano G, Giacovazzo C and Guagliardi A 1993 *J. Appl. Crystallogr.* **26** 343–50
[32] Sheldrick G M 2008 *Acta Cryst.* A **64** 112–22
[33] Farrugia L J 1999 *J. Appl. Crystallogr.* **32** 837–8
[34] Fauth F, Boer R, Gil-Ortiz F, Popescu C, Vallcorba O, Peral I, Fullá D, Benach J and Juanhuix J 2015 *Eur. Phys. J. Plus* **130** 160–72
[35] García-Saiz A, de Pedro I, Vallcorba O, Migowski P, Hernández I, Barquin L F, Abrahams I, Motevalli M, Dupont J and Gonzalez J A 2015 *RSC Adv.* **5** 60835–48
[36] Maia F, Pinto C, Waerenborgh J C, Gonçalves M A, Prazeres C, Carreira O and Sério S 2012 *Appl. Geochem.* **27** 1063–80
[37] Waerenborgh J, Rojas D, Shaula A, Mather G, Patrakeev M, Kharton V and Frade J 2005 *Mater. Lett.* **59** 1644–8
[38] Hayashi S and Hamaguchi H-O 2004 *Chem. Lett.* **33** 1590–1
[39] Chang J-C, Ho W-Y, Sun I-W, Chou Y-K, Hsieh H-H, Wu T-Y and Liang S-S 2010 *Polyhedron* **29** 2976–84
[40] Sandnes B and Rekstad J 2006 *J. Sol. Energy* **80** 616–25
[41] Busi S, Lahtinen M, Sillanpää R and Rissanen K 2006 *Acta Cryst.* C **62** 458–60
[42] Llunell M, Casanova D, Cirera J, Bofill J, Alemany P, Alvarez S, Pinsky M and Avnir D 2010 *SHAPE v1. 7* (Barcelona: University of Barcelona)
[43] Matthews R P, Welton T and Hunt P A 2014 *Phys. Chem. Chem. Phys.* **16** 3238–53
[44] Rodríguez Carvajal J 1981 *Appl. Crystallogr.* **14** 149–53
[45] Sanders-Loehr J, Wheeler W D, Shiemke A K, Averill B A and Loehr T M 1989 *J. Am. Chem. Soc.* **111** 8084–93
[46] Hart J, Rappé A, Gorun S and Upton T 1992 *Inorg. Chem.* **31** 5254–9
[47] Molins E, Roig A, Miravitlles C, Moreno-Mañas M, Vallribera A, Gálvez N and Serra N 1998 *J. Struct. Chem.* **9** 203–8
[48] Petridis D and Terzis A 1986 *Inorganica Chim. Acta* **118** 129–34
[49] Taies J A and Silver J 1986 *Inorganica Chim. Acta* **125** 67–70
[50] Greenwood N N and Gibb T C 1971 *Mössbauer Spectroscopy* (London: Chapman and Hall)